Received: 2 January 2024 | Revised: 26 June 2024 | Accepted: 5 July 2024

DOI: 10.1002/cjce.25440

RESEARCH ARTICLE

THE CANADIAN JOURNAL OF CHEMICAL ENGINEERING

Selective and efficient removal of phosphate from aqueous solution using activated carbon-supported Mg–Fe layered double oxide nanocomposites

Fisseha A. Bezza | **Hendrik G. Brink** | **Evans M. N. Chirwa**

Water Utilization and Environmental Engineering Division, Department of Chemical Engineering, University of Pretoria, Pretoria, South Africa

Correspondence
Evans M. N. Chirwa, Water Utilization and Environmental Engineering Division, Department of Chemical Engineering, University of Pretoria, Pretoria 0002, South Africa.
Email: evans.chirwa@up.ac.za

Funding information
South African Agency for Science and Technology Advancement, Grant/Award Number: IFR200206501999; Austrian Federal Ministry of Education, Science and Research (BMBWF), Grant/Award Numbers: P058, 341

Abstract

In the face of the continuous development of novel adsorbents, developing robust adsorbents with high efficiency, strong phosphate selectivity, high regenerability, and cost effectiveness is a scientific challenge. In the present study, an activated carbon-supported $MgFe_2O_4$-layered double hydroxide (AC@ $MgFe_2O_4$-LDH) derived Mg–Fe layered double oxide (AC@ $MgFe_2O_4$-LDO) nanocomposite was synthesized at various temperatures and its potential application for phosphate adsorption was investigated. The nanocomposite exhibited a hierarchical mesoporous structure with a Brunauer–Emmett–Teller (BET) specific surface area of 193 m^2/g and a narrow per-size distribution of ~2 nm. AC@$MgFe_2O_4$-LDO exhibited a high point of zero charge (pH_{pzc}) value of 9.8 and robust phosphate adsorption potential over a wide pH range of 4–9 due to its high pH buffering capacity. The effects of adsorbent dose, layered double hydroxides (LDH) calcination temperature, initial phosphate concentration, contact time, and temperature on the phosphate adsorption capacity of the adsorbent were investigated. In the present study, up to 99.0% removal of phosphate was achieved at a 4 g/L adsorbent dosage in 4 h at pH 7 and 30°C. An adsorption kinetics study revealed that the adsorption of phosphate by AC@$MgFe_2O_4$-LDO reached equilibrium within 240 min, with the kinetic experimental data fitting well with pseudo-first-order kinetics (r^2 >0.99). The Langmuir adsorption isotherm model fit the experimental data well, with a maximum adsorption capacity of 25.81 mg/g. The adsorbent displayed strong phosphate selectivity in the presence of competing anions, and the study demonstrated that AC@$MgFe_2O_4$-LDO has promising potential for efficient phosphate adsorption over a wide pH range.

KEYWORDS

activated carbon, activated carbon-supported AC@$MgFe_2O_4$-LDO, adsorption isotherm, anion exchange capacity, layered double hydroxides (LDH), phosphate adsorption

1 | INTRODUCTION

Phosphorus (P) is an indispensable nutrient for the metabolism and growth of all living organisms, as it is a significant constituent of the backbone of DNA and RNA and an integral part of energy transfer via adenosine triphosphate (ATP).[1] However, excessive discharge of phosphorus in water bodies causes eutrophication, a phenomenon leading to the growth of harmful algal blooms that pose a severe threat to human health.[2] Several established and emerging technologies have been developed for the removal of phosphate, including chemical precipitation,[3] ion exchange,[4] coagulation–precipitation,[5] adsorption,[6] membrane processes,[7] biological treatment, and combinations of both physicochemical and biological phosphate removal technologies.[8]

Adsorption is one of the most effective phosphate removal methods owing to its relatively low cost, simple operation, high efficiency, and ability to mitigate secondary pollution.[8,9] Various types of metal oxides/hydroxides, such as lanthanum (III),[10] goethite (α-FeOOH), haematite (α-Fe_2O_3), and α-FeOOH (goethite) loaded biochar,[11] and biochar layered hydroxides,[6] have been explored for the effective removal of phosphate. Activated carbon (AC) is a widely used adsorbent for wastewater treatment because of its high specific surface area, large pore volume, abundant well-developed micropores, and wide spectrum of surface functional groups.[12] Nevertheless, pristine AC has a low adsorption affinity for anionic pollutants such as phosphate due to its hydrophobicity and negative surface charge as a result of abundant oxygen-containing functional groups such as carboxyl (—COOH) and hydroxyl (—OH) groups on its surface, which undermine the binding affinity for anionic target pollutants, demonstrating little anion exchange capacity.[13] The impregnation of AC with layered double hydroxides (LDHs), such as $MnAl_2O_4$,[14] $MgFe_2O_4$,[15] and Mg/Al LDHs,[16] substantially improves the phosphate adsorption capacity of these materials.

LDHs are a class of layered materials that consist of brucite-like cationic metal hydroxide sheets, where some of the divalent metallic ions are substituted by trivalent metallic ions, giving them a net positive charge and a charge compensating interlayer exchangeable anion.[17]

LDH are represented as $[M_{1-x}^{2+}M_x^{3+}(OH)_2]^{x+}(A^{n-})_{x/n} \cdot mH_2O$, where M^{2+} and M^{3+} are divalent and trivalent cations, respectively; x is the molar ratio of $M^{3+}/(M^{2+} + M^{3+})$; and A^{n-} is the charge-balancing interlayer gallery anion.[15] High-temperature treatment of LDHs (300 to 600°C) causes destruction of the layered structure, resulting in decomposition into mixed metal oxides; the potential of these calcined products is to reconstruct the original layered structure via rehydration and simultaneous incorporation of anions into the interlayer from aqueous solution, resulting in superior anion scavenging capacity.[15,17] The memory effect, capacity to recover the original layered structure by the rehydration of calcined LDH products, and high ion exchange potential contribute to the efficient anionic pollutant adsorption potential of LDHs.[15,17] LDHs and their calcined oxides have been reported to efficiently adsorb hazardous anionic pollutants due to their large surface area (20–120 m^2/g), high anion exchange capacity (3.0–4.8 meq/g), Bronsted-Lewis acidity and basicity, memory effect, and low anion selectivity.[18] LDHs have demonstrated efficient phosphate adsorption potential[14,19]; however, the phosphate adsorption performance of bare/granular LDHs is adversely affected owing to their very tight and multilayered stacking and aggregation.[14,20] Dispersions of LDHs onto high surface areas and porous AC substrates are suggested to synergistically maximize the sorption capacity of composites for various anionic contaminants, including phosphates.[6,14,21] In the present study, AC-supported $Mg^{II}Fe^{III}$-layered double oxide (AC@ Mg–Fe LDO) was derived from Mg–Fe LDH at calcination temperatures of 200, 400, and 600°C, and its phosphate adsorption potential was investigated. In addition to the effect of calcination temperature, the pH of the solution and adsorbent dosage were assessed for their effect on the phosphate adsorption potential of the AC@ Mg–Fe layered double oxides (LDO).

2 | MATERIALS AND METHODS

2.1 | Materials

Finely ground commercial AC, magnesium chloride hexahydrate ($MgCl_2 \cdot 6H_2O$; 98%), ferric chloride hexahydrate ($FeCl_3 \cdot 6H_2O$; 99%), and potassium phosphate monobasic (KH_2PO_4, 98%) were obtained from Sigma–Aldrich.

2.2 | Synthesis of AC-supported $MgFe_2O_4$-LDH

$MgFe_2O_4$-LDHs with a Mg/Fe molar ratio of 2 was prepared by coprecipitation at a fixed pH of 12, as previously described by Jiménez-López et al.[22] Briefly, an aqueous solution was prepared by mixing 0.2 mol of $MgCl_2 \cdot 6H_2O$ and 0.1 mol of $FeCl_3 \cdot 6H_2O$ in 100 mL of ultrapure deionized water and labelled solution A. Another solution was prepared by adding 0.25 mol of NaOH and 5 g of AC in 100 mL of deionized water and mixing by ultrasonication for half an hour to obtain solution (B). The AC was treated in 3 M HCl for 2 h, washed with deionized water and dried at 110°C in an

oven to remove impurities. This procedure was repeated twice until no further weight loss was observed. Solution A of the metal chlorides was slowly poured into solution B of NaOH containing 5 g of AC (pH ≈12) under vigorous stirring. During the coprecipitation process, the pH was monitored and maintained at a constant value equal to 12 by the addition of 3 M NaOH solution. The slurry was stirred vigorously for 2 h at 80°C, aged for 6 h, and then collected by centrifugation. The obtained material was washed with distilled water repeatedly until the solution pH was neutral, and until Cl^- free LDH-functionalized AC was obtained, the mixture was vacuum dried for 24 h at 105°C, calcined at 200, 400, and 600°C for 4 h under flowing nitrogen gas, allowed to cool at room temperature (approximately 27°C), and used for the adsorption study. Assuming complete precipitation of the Mg and Fe salts and formation of the $MgFe_2O_2$, the final AC/$MgFe_2O_2$ product will have AC to $MgFe_2O_2$ mass ratio of 1/3.

2.3 | Material characterization

To evaluate the pore structure, surface area, and functional groups present in the pristine AC and AC-supported $MgFe_2O_4$-LDH (AC@$MgFe_2O_4$-LDH) nanocomposites, surface area analysis and Fourier transform infrared (FTIR) characterization were conducted.

To determine the crystalline nature of the synthesized nanoparticles, X-ray diffraction (XRD) patterns of the as-prepared samples were obtained using a PANalytical X'Pert Pro powder diffractometer in the θ–θ configuration with an X'Celerator detector equipped with Cu-Kα radiation ($\lambda = 1.54$ Å) operated at 45 kV/200 mA and a scan speed of 1.0°/min in the 2θ range of 5°–70°. The mineralogy was determined by selecting the best–fitting pattern from the ICSD database to the measured diffraction pattern using X'Pert Highscore plus software. The relative phase amounts (wt.%) were estimated using the Rietveld method (X'Pert Highscore Software). The particle size and morphology of the materials were examined using transmission electron microscopy (TEM, JOEL JEM-2100F) at an acceleration voltage of 200 kV. The surface morphology and localized elemental composition of the as-prepared nanoparticles were simultaneously analyzed via high-resolution Zeiss Ultra Plus 55 field emission scanning electron microscopy (FE-SEM) with energy dispersive X-ray spectroscopy (EDS) operated at an acceleration voltage of 2.0 kV. A thin layer of sample was spread on an SEM stub mount and covered with a ∼ 10 nm nickel film for analysis. The surface functional groups of the nanoparticles were analyzed using a FTIR spectrometer (FTIR, Perkin Elmer-400 Series). FTIR spectra were recorded at room temperature using KBr pellets in the frequency range of 4000 to 400 cm^{-1} at a resolution of 4 cm^{-1}. To obtain a good signal-to-noise ratio, 32 scans were run and averaged.

Nitrogen adsorption–desorption isotherms were obtained at 77 K using volumetric adsorption–desorption measurements (Micromeritics ASAP 2460). Prior to the volumetric adsorption/desorption measurements, the samples were preheated and degassed under vacuum at 150°C for 18 h. The specific surface area (S_{BET}) of the samples was determined using the Brunauer–Emmett–Teller (BET) equation with nitrogen adsorption data at a relative pressure range of $0.1 < P/P_0 < 0.35$. The total pore volume (V_{tot}) was obtained from the amount of nitrogen adsorbed at $P/P_0 = 0.95$. The density functional theory (DFT) method was used to determine the pore size distribution (PSD) of the samples.[23]

2.4 | Batch adsorption study

A stock solution of 1000 mg/L phosphate was prepared by dissolving 4.39 g of KH_2PO_4 in 1 L of distilled water and diluting to the required concentration using distilled water. Batch adsorption studies were carried out in a series of 250 mL Erlenmeyer volumetric flasks containing 100 mL of a solution of phosphate ranging from 5 to 200 mg/L at various adsorbent dosages, solution pH values, initial phosphate concentrations, contact times, and temperatures to examine the influence of the parameters on the adsorption performance of the adsorbent. The effect of the calcination temperature on the phosphate adsorption potential was studied using 4 g/L adsorbent calcined at various temperatures (400, 500, and 600°C). The solution pH was adjusted from 3.0 to 11.0 by using 0.5 M HCl and 3 M NaOH. The flasks were then placed on an orbital temperature-controlled shaker with a shaking speed of 200 rpm at various temperatures (20, 30, and 40°C). An equilibrium adsorption isotherm study was conducted over initial phosphate concentrations ranging from 5 to 200 mg/L at 4 g/L adsorbent dosage and pH 5 ± 0.5 at 30°C for 480 min, which was determined to be sufficient time to reach equilibrium from the preliminary test. Adsorption kinetics studies were performed by agitating phosphate solution at an initial concentration of 120 mg/L at pH 5 ± 0.5 and an adsorbent dosage of 4 g/L by collecting samples at 30-minute intervals for 480 min. A thermodynamic study of phosphate adsorption was carried out at various temperatures (20, 30, and 40°C) with an initial phosphate concentration of 120 mg/L, an adsorbent dose of 4 g/L, and a pH of 5 for 360 min. To study the effect of competing ions on phosphate adsorption, 4 g/L adsorbent was added to 100 mL of 40.0 mg P/L phosphate solution containing 20 mg/L CO_3^{2-}, F^-, SO_4^{2}, or NO_3^- anions prepared by dissolving

sodium salts of the respective anions at pH 5 for 360 min. Periodically, 5 mL samples were withdrawn and centrifuged at 5000 rpm for 3 min and syringe filtered (0.45 μL syringe filter), and the residual phosphate concentration was determined by the molybdenum blue calorimetric method.[24,25,26] Briefly 5 mL of aqueous phosphate solution was mixed with 5 mL mixed reagent consisting of antimony potassium tartrate (0.009 M), sulphuric acid (2.5 M), and ammonium molybdate (0.033 M) and subjected to 5 mL ascorbic acid (0.1 M) reduction. The intensity of the molybdenum blue complex formed was determined by measuring its absorbance using UV Vis spectrophotometer at 860 nm and correlated with a standard calibration curve generated from known phosphate concentrations.

To study the effects of various parameters, one parameter was changed at a time while keeping the rest constant. All the experiments were performed in triplicate at 30°C unless otherwise stated, and the data are presented as the means ± SDs. The percentage removal ($R\%$) and adsorption capacity (mg phosphate/g) of AC@$MgFe_2O_4$ LDO at time t (q_t) and equilibrium (q_e) were calculated using formulas 1, 2, and 3. Control experiments were carried out using pristine AC under the same conditions to compare the performances of the two adsorbents.

$$\text{Percentage removal}\,(\%R) = \frac{C_i - C_t}{C_i} \times 100\% \quad (1)$$

$$\text{Adsorption capacity at equilibrium}\,(q_e) = \frac{(C_i - C_e)}{m} \times V \quad (2)$$

$$\text{Adsorption capacity at time}\,t\,(q_t) = \frac{(C_i - C_t)}{m} \times V \quad (3)$$

where C_i, C_e, and C_t represent the initial concentration, equilibrium concentration, and concentration at time t (mg/L), respectively; V (L) is the solution volume and m (g) is the mass of the AC@$MgFe_2O_4$ LDO nanocomposite.

2.5 | Measurements of the point of zero charge (pH_{PZC})

The pH at the point of zero charge (pH_{PZC}) was determined as previously described by Park et al.[27] Briefly, 500 mg of AC@$MgFe_2O_4$ LDO composite was added to 100 mL of 0.1 M NaCl, and the initial pH was adjusted to 3 to 11 with 3 M HCl and NaOH solutions. The vails were sealed and shaken for 24 h at 200 rpm and at room temperature. Subsequently, the final pH was measured and plotted against the $pH_{initial} - pH_{final}$, ΔpH, and then, the pH at which $pH_{initial} = pH_{final}$ is the point of zero charge, pH_{pzc}. The average values of three measurements were calculated, and the mean ± SD are reported.

2.6 | Adsorbent regeneration and phosphate recovery

The regeneration efficiency, defined as the ratio of the adsorption capacity of the regenerated adsorbent to that of the fresh adsorbent, was used to evaluate the regeneration performance of the adsorbent. Adsorbent regeneration was conducted using 1 M NaOH with slight modifications to the method previously described by Zach-Maor et al.[28] Briefly, adsorption was conducted with an initial phosphate concentration of 100 mg/L and an adsorbent dosage of 4 g/L for 540 min; then, the adsorbent was collected by centrifugation (10,000 rpm, 5 min). Subsequently, the adsorbent was eluted with 1 M NaOH adjusted to a pH of 13 through shaking for 12 h. The adsorbent was collected through centrifugation, washed with deionized water, and vacuum dried at 100°C for 6 h. The regenerated adsorbent was used for further adsorption studies, and adsorption/desorption cycles were carried out six times.

3 | RESULTS AND DISCUSSION

3.1 | Characterization of the adsorbent

The phase composition and crystallinity of the LDH precursor and LDOs obtained at different calcination temperatures were studied using XRD analysis. The XRD diffraction patterns of the AC@$MgFe_2O_4$ LDH and AC@$MgFe_2O_4$ LDO nanocomposites obtained before and after calcination at various temperatures are presented in Figure 1. The diffraction peaks of the as-synthesized sample at 11.4°, 22.7°, 34.2°, 38.8°, and 60.9° observed before the calcination of AC@$MgFe_2O_4$LDH corresponded to the (003), (006), (009), (012), and (110) crystal planes of AC@$MgFe_2O_4$LDH, respectively.[29] The nanocomposite samples calcined at increasing temperatures displayed well-defined diffraction peaks at 2θ values of 30.5°, 35.5°, 43.5°, 53.5, 56.5°, and 62.6°, which corresponded to the (220), (311), (222), (400), (422), (511), and (440) crystal planes, respectively, and were attributed to the $MgFe_2O_4$ LDO (matched with JCPDS 71–1232).[30] After calcination, the XRD patterns of the AC@$MgFe_2O_4$LDH samples showed entirely different patterns, signifying the collapse of the LDH structure and the formation of mixed metallic oxides as well as $MgFe_2O_4$ spinel.[29]

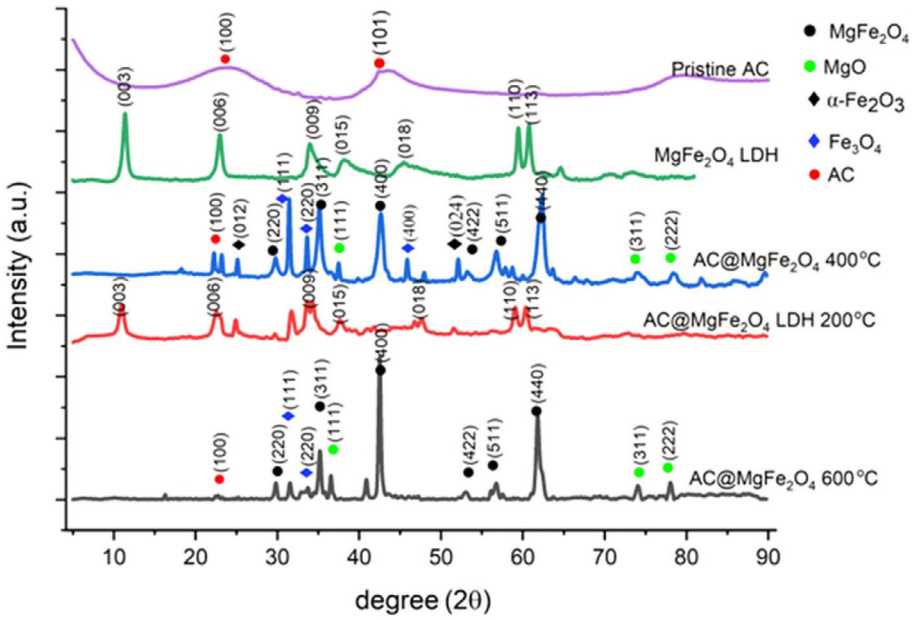

FIGURE 1 X-ray diffraction patterns of activated carbon-supported $MgFe_2O_4$-layered double hydroxide (AC@ $MgFe_2O_4$-LDH) and its calcined products (Mg–Fe layered double oxide [AC@ $MgFe_2O_4$-LDO]) calcined at different temperatures.

As displayed in Figure 1, the crystallinity and phase purity increased with increasing calcination temperature from 200 to 600°C. The spectral peaks at 2θ values of 31.2°, 33.6°, and 46° can be ascribed to the (111), (220), and (400) diffraction planes of Fe_3O_4, which are much lower in high-temperature calcined samples than in low-temperature calcined samples.[31] The diffraction peaks at 37.01°, 74.87°, and 78.82° correspond to the characteristic (111), (311), and (222) crystal planes of MgO, respectively (JCPDS file no. 65-0476).[32] Additional peaks corresponding to the haematite (α-Fe_2O_3) phase were observed in the XRD patterns, indicating the presence of a significant amount of α-Fe_2O_3 in the 450°C calcined sample. Pristine AC displayed diffraction peaks at 2θ values of 23.5° and 43.1° correspond to the (100) and (101) crystal planes of AC, respectively (JCPDS number 75–2078). The $MgFe_2O_4$ displayed peaks at 11.4°, 22.7°, 34.2°, 38.8°, and 60.9° corresponding to the (003), (006), (009), (012), and (110) crystal planes of $MgFe_2O_4$LDH, respectively.[29] The calcination of LDH produces mixed highly reactive mixed metallic oxides, also called LDOs.[33] Calcination of LDHs from 300 to 600°C results in the progressive loss of interlaminar anions and water molecules and the formation of LDOs, which are characterized by a high specific surface area resulting from the development of porous structures through gasification processes, thermostability, and pore volume.[34]

The FTIR spectra of AC@$MgFe_2O_4$-LDH and AC@$MgFe_2O_4$-LDO (calcined at 200, 400, and 600°C) are shown in Figure 2A. The peaks observed at ~543 and ~441 cm^{-1} are assigned to tetrahedral and octahedral complexes, respectively, which signifies the formation of the $MgFe_2O_4$ LDH structure.[24,25] The higher frequency band (ν_1) (543 cm^{-1}) and lower frequency band (ν_2) (441 cm^{-1}) are assigned to the tetrahedral and octahedral complexes of $MgFe_2O_4$-LDH.[35]

The FTIR spectrum of AC@$MgFe_2O_4$-LDH in the region from 1400 to 1600 cm^{-1} may be ascribed to the presence of aromatic (C═C) or benzene rings and various substitution modes of the aromatic rings.[36] The absorption band at ~1354 cm^{-1} is attributed to the bending vibration of the hydroxyl group.[37] The broadband peaks in the range of 1000 to 1300 cm^{-1} are ascribed to C—O stretching in carboxylic acid, anhydride, phenol, ether, and ester groups.[38] The surface of AC@$MgFe_2O_4$-LDH was observed to have diverse functional groups, among which C—O-type groups were predominant and formed carboxylic acids, anhydrides, phenols, and ethers (1106 cm^{-1}).

Further FTIR characterization of the pristine AC and $MgFe_2O_4$ was conducted to gain insights into the intrinsic characteristics as well as the functional groups and bonds present in each component. The FTIR analysis of the AC revealed numerous functional groups, as depicted in Figure 2B. The broad peak ranging from 3200 to 3400 cm^{-1} is indicative of the OH-stretching vibration associated with hydroxyl functional groups.[39] The band at around 1446 cm^{-1} can be assigned to the C—H deformation modes of CH_2 groups.[40] The bands at 1100 and 1353 cm^{-1} can be ascribed to the C—O stretching vibrations of the functional groups either from ether, ester, or phenol,[38,41] whereas the band observed appearing at around 860 cm^{-1} is assigned for C—C stretching. In short, the functional groups observed on the AC included phenols, hydroxyl, carboxyl, and carbonyl groups. Another band appearing at around 873 cm^{-1} indicates the stretching of C—C bonds. The AC sample displayed functional groups such as phenols, hydroxyl,

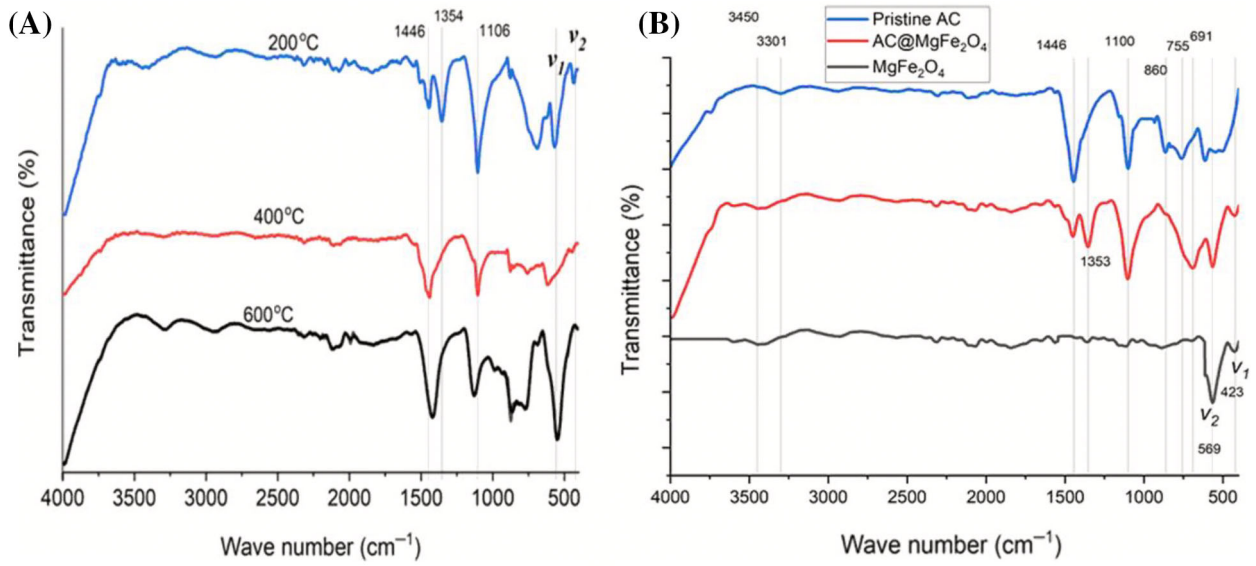

FIGURE 2 (A) Fourier transform infrared (FTIR) spectra of activated carbon-supported $MgFe_2O_4$-layered double hydroxide (AC@$MgFe_2O_4$-LDH) and the activated carbon-supported Mg–Fe layered double oxide (AC@$MgFe_2O_4$ LDO) calcined at different temperatures. (B) FTIR spectra of the pristine AC, $MgFe_2O_4$, and AC@$MgFe_2O_4$ calcined at 400°C.

carboxyl, and carbonyl groups.[42] The $MgFe_2O_4$ showed sharp peaks at 423 and 569 cm^{-1}, assigned to the stretching vibrational metal oxide modes of Mg—O and Fe—O bonds in $MgFe_2O_4$, indicating the successful formation of the $MgFe_2O_4$ LDH structure.[43] The bands around 3450 cm^{-1} represent OH-stretching vibration of hydroxyl functional groups indicating the presence of absorbed or free water in the sample.[39] The study confirms the preservation of the various oxygen-containing functional groups in the AC@$MgFe_2O_4$, which are the intrinsic characteristics of the original AC that greatly enhance the reactivity and adsorption capacity of the AC@$MgFe_2O_4$.

Nitrogen adsorption/desorption analyses of the AC@$MgFe_2O_4$-LDH nanocomposite and pristine AC exhibited type IV isotherms, with H1 hysteresis loops in the relative pressure (P/P_0) range of 0.4–0.9, as presented in Figure 3A–D, respectively, which are indicative of the presence of mesoporous structures.[44]

The Figure 3A,B insets show the PSDs of the AC@$MgFe_2O_4$-LDO nanocomposites and pristine AC samples, respectively, over the range of 1 to 9 nm, as determined using DFT. The PSD exhibited a maximum curve at a ~2 nm pore radius, indicating the mesoporosity of the material. As presented in Table 1, the BET specific surface area and pore volume of the AC@$MgFe_2O_4$-LDO nanocomposite were determined to be 193 m^2/g with a corresponding pore volume of 0.16 cm^3/g, while the pristine AC exhibited a larger surface area of ~616.11 m^2/g with a corresponding pore volume of 0.48 cm^3/g. The decrease in the surface area of the AC upon loading $MgFe_2O_4$ nanoparticles is indicative of the filling of pores on the AC matrix, which provides less available surface area for nitrogen adsorption. The increase in the amount adsorbed at a relative pressure of $P/P_0 = 0.3$–0.9 indicates the presence of mesopores that account for the high porosity and versatility of the adsorbent for diverse applications, including the adsorption of pollutants. The impact of post-synthesis calcination temperature on the AC@$MgFe_2O_4$LDH surface area and porosity was evaluated by analyzing the BET surface area and pore volume of the samples at various temperatures. The results, illustrated in Figure 4 and Table 1, revealed a decrease in BET surface area from 194.33 to 165.67 and 110.54 m^2/g, respectively, as the calcination temperature decreased from 600 to 400°C and 200°C, respectively, leading to reduced porosity and pore volume as shown in Table 1. This observation reveals progressive loss of interlaminar anions and water molecules and the formation of LDOs, which are characterized by a high specific surface area resulting from the development of porous structures through gasification processes, thermostability, and pore volume.[34] In the subsequent morphological and physicochemical characterization studies, the AC@$MgFe_2O_4$LDO sample calcined at 600°C was used. The performance of the samples calcined at the different temperatures was carried out to assess the performance of the sample calcined at 600°C compared to the other two samples calcined at 200 and 400°C.

A comparison of the PSD of the $MgFe_2O_4$-LDO nanocomposites calcined at different temperatures as well as with that of the pristine AC revealed that impregnation

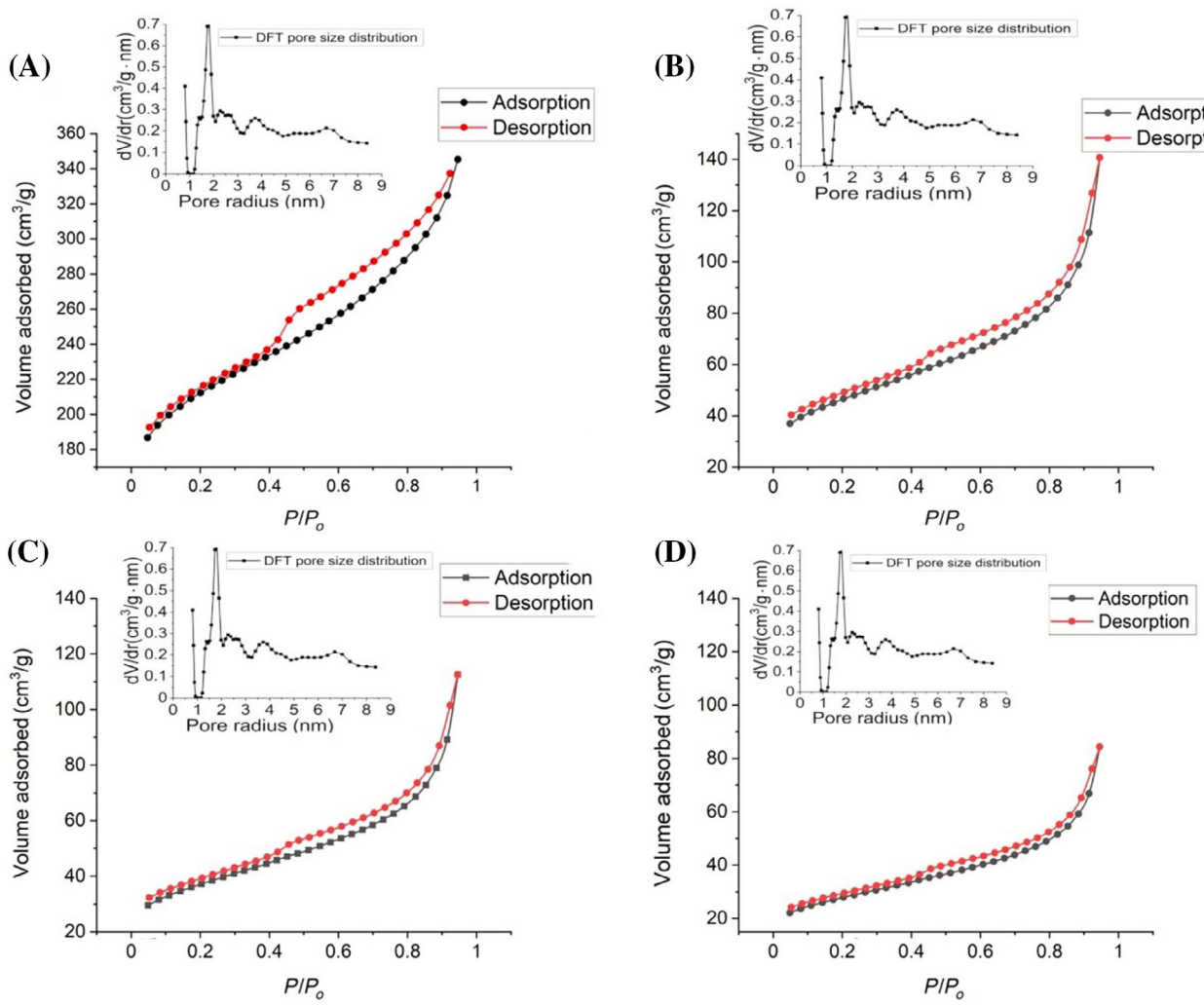

FIGURE 3 (A) N_2 adsorption/desorption isotherms of pristine activated carbon (AC); (B) activated carbon-supported Mg–Fe layered double oxide (AC@$MgFe_2O_4$ LDO) nanocomposite adsorbent calcined at 600°C; (C) AC@$MgFe_2O_4$-LDO nanocomposite adsorbent calcined at 400°C; (D) AC@$MgFe_2O_4$-LDO nanocomposite adsorbent calcined at 200°C and (insets) their corresponding density functional theory (DFT) pore size distribution (PSD) curves.

TABLE 1 The Brunauer–Emmett–Teller (BET) surface area and total pore volume of the adsorbents were determined from nitrogen adsorption/desorption isotherms.

Adsorbent	BET surface area (m^2/g)	Total pore volume (cm^3/g)
Pristine activated carbon (AC)	616.11	0.48
AC@$MgFe_2O_4$ calcined at 600°C	193.33	0.16
AC@$MgFe_2O_4$ calcined at 400°C	165.67	0.13
AC@$MgFe_2O_4$ calcined at 200°C	110.54	0.06

of the AC with $MgFe_2O_4$ did not affect the mesoporosity of the AC in all cases. The preservation of the mesoporosity of nanocomposites after loading NPs is highly important, as mesoporous nanocomposites, which have pore sizes between 2 and 50 nm, are appealing porous materials for efficient adsorption of various adsorbates.[45]

Figure 4 displays FESEM images of pristine AC and AC@$MgFe_2O_4$-LDO nanocomposites at different magnifications.

Figure 4A,B show the morphologies of the pristine AC and AC@$MgFe_2O_4$-LDO nanocomposites, respectively. A comparison of the AC and AC@$MgFe_2O_4$-LDO nanocomposite images at this particular magnification revealed no significant distinction in their morphology, demonstrating the well-embedded and uniform distribution of the nanoparticles on the AC surface. Porous AC, with its high surface area and large pore volume, serves as a scaffold to prevent particle aggregation through special confinement of nanoparticle growth in its pores, thereby limiting particle size. As shown in Figure 4C,D, a closer look at the SEM micrograph at a higher magnification reveals the

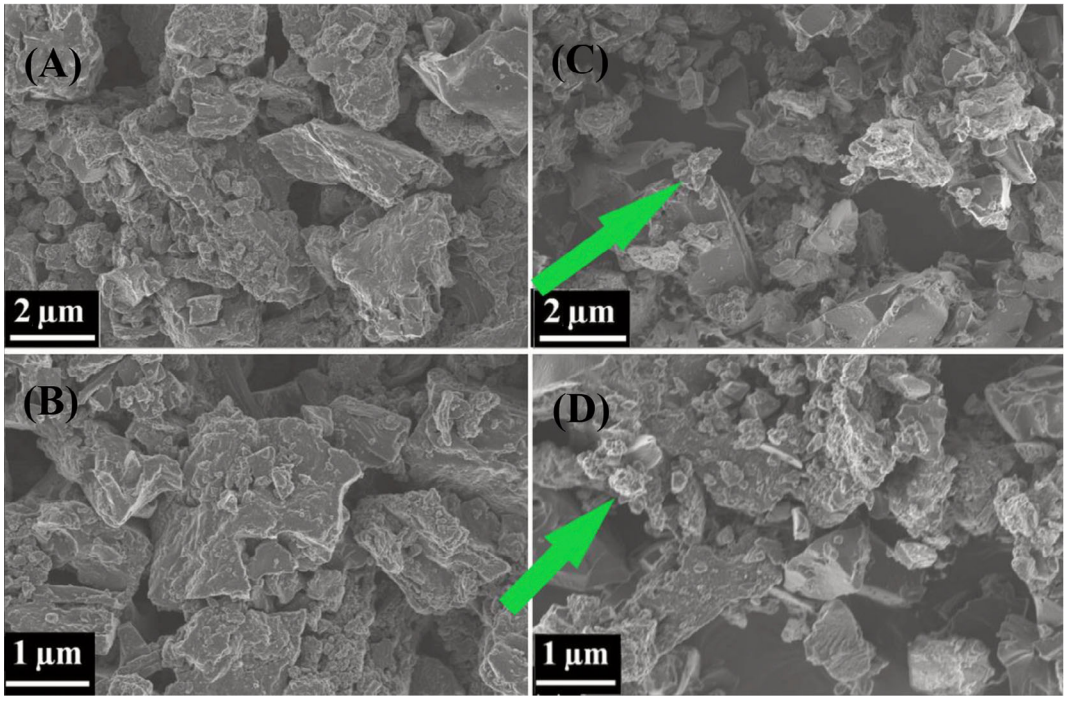

FIGURE 4 (A,B) Scanning electron microscopy images of pristine activated carbon and (C,D) the activated carbon-supported $MgFe_2O_4$-layered double hydroxide (AC@$MgFe_2O_4$-LDO) nanocomposites at different magnifications.

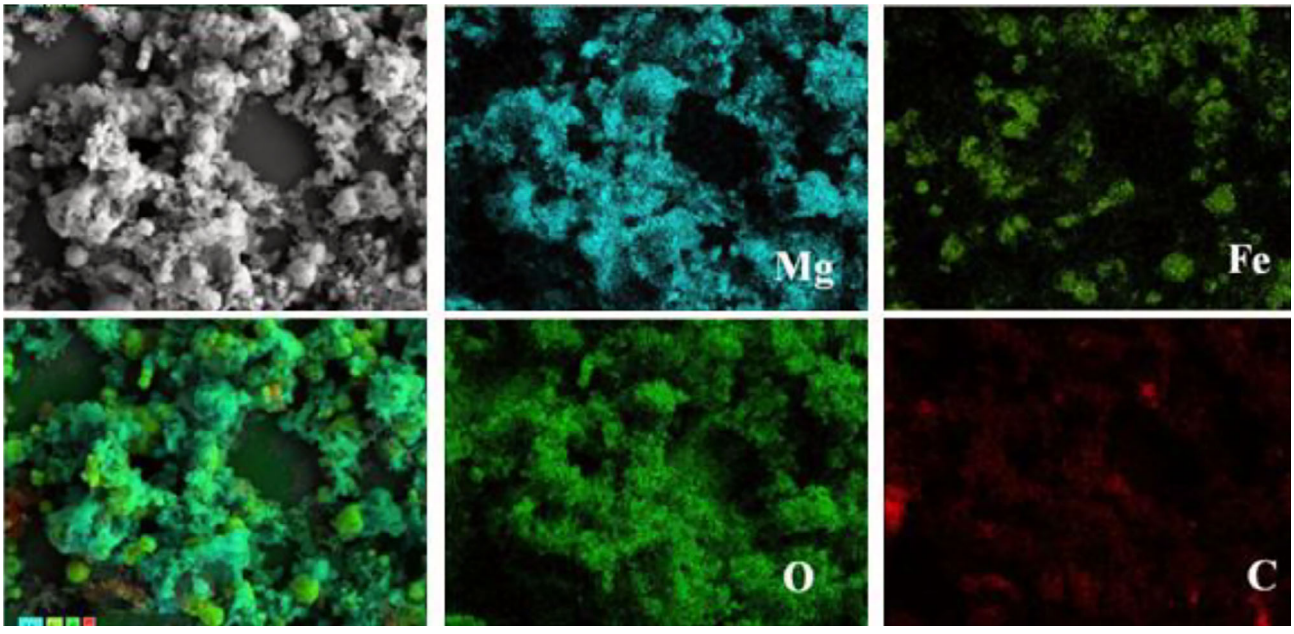

FIGURE 5 Energy dispersive x-ray spectroscopy elemental mapping of Mg, Fe, O, and C in the activated carbon-supported $MgFe_2O_4$-layered double hydroxide (AC@ $MgFe_2O_4$-LDH) nanocomposites on the porous matrix of the activated carbon.

tetrahedral structure of the $MgFe_2O_4$ nanoparticles embedded in the porous carbon scaffolds (indicated by *green arrows*).

EDX elemental mapping was performed on a cross-section, as shown in Figure 5, revealing that the Fe, O, and Mg were dispersed uniformly throughout the whole porous structure of the AC. This confirms that small $MgFe_2O_4$ nanoparticles are formed on the porous AC support and are homogeneously distributed throughout the AC pore matrix.

3.2 | Effect of calcination temperature and dosage of the LDO adsorbents

The calcination of LDH in the temperature range from 300 to 600°C releases laminar anions and water molecules, resulting in thermal decomposition and the formation of highly reactive LDOs.[46] The impact of calcination temperature on the phosphate adsorption potential of LDO samples was studied by calcining the LDH samples at various temperatures (200, 400, and 600°C) for 4 h. The effect of adsorbent dose on phosphate adsorption was studied using various dosages of the AC@$MgFe_2O_4$ LDO nanocomposite (2, 4, 6 g/L) calcined at 600°C at pH 7. The amount of phosphate adsorbed increased from ~70.5% to ~99.5% and exhibited a slight reduction to ~96.5% as the adsorbent dosage increased from 2 g/L to 4 and 6 g/L, respectively (Figure 6A), at the end of 4 h of adsorption. The increase in the adsorption process observed, which was proportional to the adsorbent dose, may be attributed to the increasing number of adsorption sites and available surface area for phosphate adsorption.[47] However, a further increase in adsorbent dosage from 4 to 6 g/L slightly reduced the adsorption performance, which could be ascribed to the overlap of adsorption sites.[48]

As displayed in Figure 6B, the highest adsorption performance, reaching 99%, was observed at 600°C, with lower adsorption performances occurring at 200 and 400°C calcination temperatures. The high adsorption performance of the LDO mixed oxides at higher calcination temperatures can be attributed to the well-developed high porosity, high specific surface area, large pore volume, and appropriate pore size characteristics of the LDO, which provide a high concentration of active adsorption sites for efficient adsorption, basic property of MgO, and exposed interlaminar sites for rapid diffusion into the interior of the adsorber.[49]

As previously observed via XRD analysis, $MgFe_2O_4$-LDH underwent thermal decomposition at 300–600°C to produce porous mixed metal oxides of Fe_3O_4, α-Fe_2O_3, MgO, and the $MgFe_2O_4$ spinel phase at higher temperatures. The AC@$MgFe_2O_4$ LDOs spontaneously restored their original layered structure and turned into LDHs when LDOs entered aqueous solution, where they adsorbed water molecules and anions. The simultaneous reconstruction of the LDH structure from the LDO upon entering aqueous solution and adsorbing anions, which is called the 'memory effect', is generally believed to be an important factor for the efficient adsorption of anions through the high anion exchange potential of LDHs.[22,50,51] The LDO obtained at 600°C calcination and a dose of 4 g/L was used for further adsorption studies.

3.3 | Effect of solution pH

The pH of a solution plays a significant role in the adsorption of phosphate. The solution pH affects adsorption because it governs the ionization of phosphate ions into dihydrogen phosphate ($H_2PO_4^-$), monohydrogen phosphate (HPO_4^{2-}), and orthophosphate (PO_4^{3-}), as well as functional groups on the adsorbent surface at different pH values.[52] The optimal pH for adsorption was studied through an investigation of the adsorption performance over a range

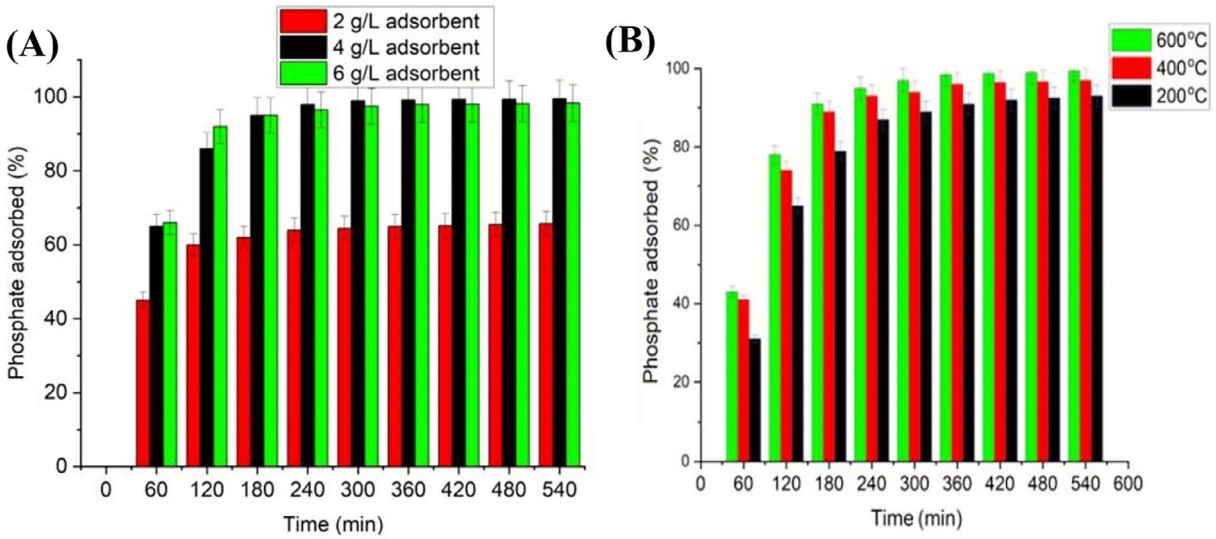

FIGURE 6 (A) Effect of adsorbent dose on the adsorption of phosphate at pH 5, 30°C, and an initial phosphate concentration of 120 mg/L; (B) effect of calcination temperature on the removal of phosphate at an initial concentration of 120 mg/L by activated carbon-supported Mg–Fe layered double oxide (AC@$MgFe_2O_4$ LDO) at a 4 g/L adsorbent dose at 30°C.

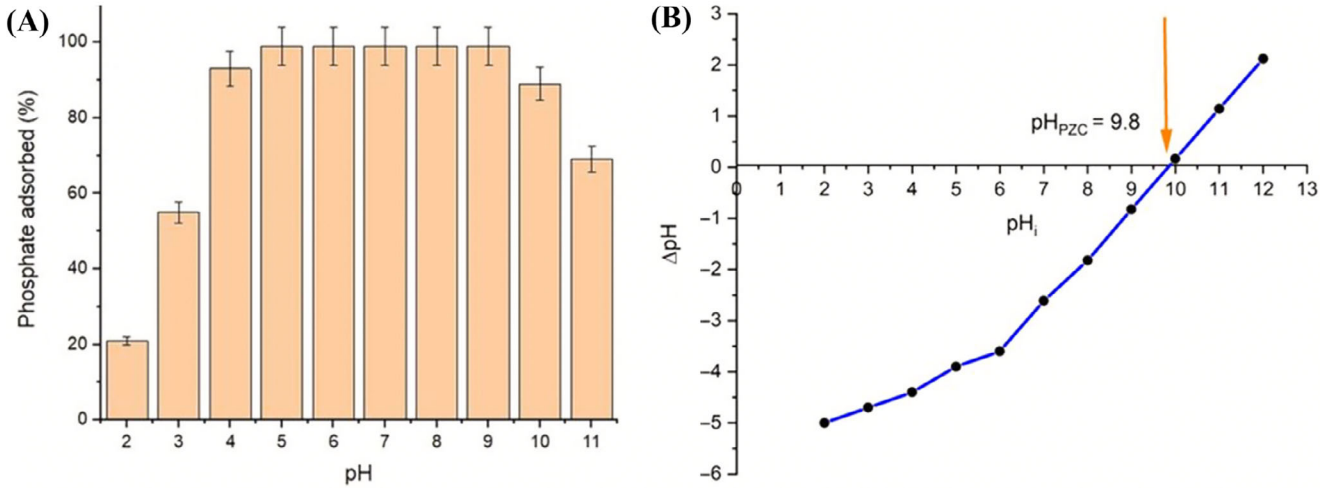

FIGURE 7 (A) Effect of pH on the adsorptive removal of phosphate at an initial concentration of 120 mg/L by activated carbon-supported Mg–Fe layered double oxide (AC@$MgFe_2O_4$ LDO) at a 4 g/L adsorbent dose at 30°C. (B) Profile of point of zero charge (pH_{PZC}) of AC@$MgFe_2O_4$-LDO.

of pH values (3–11). As presented in Figure 7A, the percentage of phosphate adsorbed increased from 55.5% to 99.10% as the pH increased from 3 to 5 and did not significantly change as the pH increased to 9. The initial solution pH significantly affects the phosphate adsorption potential of an adsorbent by influencing the charge of the adsorbent surface, which is determined through the study of the point of zero charge (pH_{ZPC}), which is the pH at which the adsorbent surface is neutral.[53] The pHpzc of the AC@$MgFe_2O_4$ was determined to be 9.8 as presented in Figure 7B. At pH values <pH_{pzc}, the adsorbent develops a positive surface charge, whereas at pH > pHpzc, the superficial charges of the material become negatively charged.[54] The maximum adsorption capacity observed in Figure 7A is attributed to the electrostatic attraction between the negatively charged phosphate anions and the positively charged surface of the AC@$MgFe_2O_4$ adsorbent (pH < pH_{ZPC}). The surface anion group of the LDH could be exchanged by the adsorbed phosphate anions, forming PO_4 inner-sphere complexes via a ligand substitution reaction on the adsorbent surface. However, increasing the solution pH increases the number of hydroxyl groups, thus increasing the number of negatively charged sites and affecting the attraction between phosphate anions and the adsorbent surface.[55] Phosphate is a polyprotic acid and has pK values of 2.12, 7.21, and 12.67; depending on the solution pH, it can exist in the form of H_3PO_4, dihydrogen phosphate ($H_2PO_4^-$), monohydrogen phosphate (HPO_4^{2-}), or orthophosphate (PO_4^{3-}) in water.[56] From the data presented in Figure 7B, the maximum adsorption capacity of phosphate was found at pH values ranging from 4 to 9, which may be attributed to the high pH buffering capacity of LDO.[52] Nonetheless, the adsorption capacity decreases in a strongly acidic environment (pH <4), which may be attributed to protonation of dihydric phosphate to produce neutral phosphoric acid molecules (H_3PO_4, pKa 2.1), which cannot be absorbed by the protonated adsorbent or by leaching of the $MgFe_2O_4$ structure under strongly acidic conditions.[19,48] At higher pH values (pH >9.8), the surface of the adsorbent will be negatively charged due to the deprotonation of organic groups on the surface or adsorption of OH, causing repulsion between the phosphate ions and hydroxyl ions on the surface of the adsorbent. Thus, compared to the results of several studies, the LDH functionalization of AC favoured the adsorption of phosphates over a wide range of pH values with no significant change in adsorption efficiency.

Similar studies were carried out using pristine AC as an adsorbent under the same experimental conditions. The results of the adsorption study showed that pristine AC could achieve up to ~95% adsorption of phosphate at a lower pH range (Figure S1). However, pristine AC was less effective at adsorbing phosphate than was AC@$MgFe_2O_4$ LDO, which demonstrated almost complete adsorption of phosphate over a broad pH range. Despite the mesoporous structure, large surface area, and abundance of functional groups, such as aromatic and oxygen-containing functional groups, such as carboxylic acid, carbonyl, phenol, lactose, and ester groups (Figure S2), the phosphate adsorption performance of pristine AC is inferior to that of AC@$MgFe_2O_4$ LDO. The lower adsorption affinity of pristine AC may be attributed to its hydrophobicity and negative surface charge due to the abundant oxygen-containing functional groups (such as carboxyl [—COOH] and hydroxyl [—OH] groups) on the surface, which undermine the binding

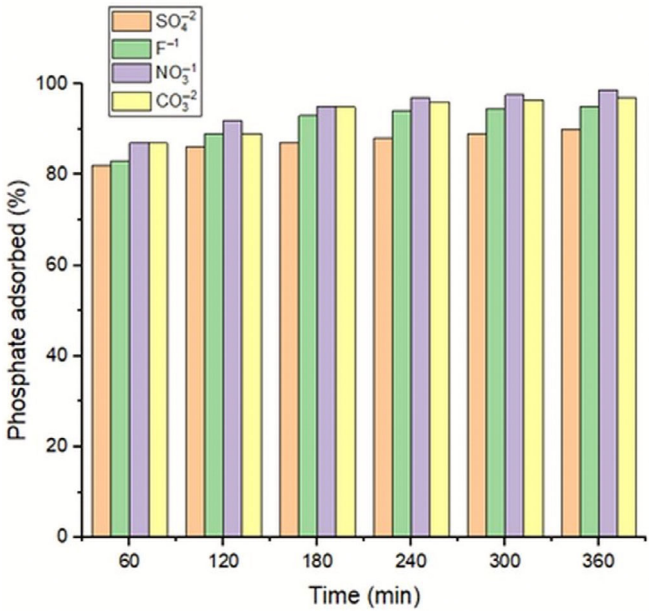

FIGURE 8 Effect of coexisting anions on phosphate adsorption at an initial phosphate concentration of 100 mg/L and a coexisting anion concentration of 20 mg/L at an adsorbent dose of 4 g/L and pH 5 for 360 min.

affinity toward anionic target pollutants, demonstrating little anion exchange capacity.[57] The predominant functional groups in the AC were hydrophobic aliphatic and aromatic hydrocarbons, along with oxygen-containing functional groups, causing repulsion of anions and resulting in less effective performance compared to that of the AC@$MgFe_2O_4$ LDO.

3.4 | Effect of coexistent ions

Owing to the coexistence of various anions in municipal and industrial wastewaters that compete for adsorption sites, determining the competitive inhibitory effect of coexisting anions on phosphate adsorption is critically important. The study demonstrated that the multivalent anion SO_4^{2-} exhibited up to a 10% reduction in phosphate adsorption at a concentration of 20 mg/L, followed by the F^- anion, which exhibited up to 5% inhibition of phosphate adsorption on AC@$MgFe_2O_4$-LDO. The other multivalent CO_3^{2-} and monovalent NO_3^- anions inhibited phosphate adsorption on AC@$MgFe_2O_4$-LDO by less than 2% at the end of 6 h of adsorption (Figure 8). The greater competitive inhibition of the multivalent SO_4^{2-} anion may be attributed to its higher charge density than that of the monovalent ions.[58] The greater inhibitory effect of fluoride ions on the other monovalent ions can be ascribed to their strong electronegativity, which enables them to easily take up protonated adsorption sites, resulting in a continual decrease in phosphate adsorption as the concentration of fluoride increases.[59] However, the adsorbent demonstrated significant selectivity for phosphate anions in the presence of various coexisting anions, demonstrating its greater affinity for phosphate ions and its robust adsorption performance.

3.5 | Adsorption isotherms

Equilibrium adsorption isotherms reveal the correlation between the adsorption capacity of an adsorbent (q_e) and the equilibrium concentration (c_e) of an adsorbate at constant temperature and assist in determining the adsorption mechanisms, adsorbent surface properties, and nature of the adsorbate.[60] The investigation of equilibrium adsorption isotherms is fundamentally important for the design, scaling up, and efficient operation of adsorption processes that require equilibrium adsorption data for use in kinetic and mass transfer models.[55] In the present study, adsorption isotherms were analyzed according to the Langmuir and Freundlich adsorption model equations. Equations (4) and (5), respectively.

$$q_e = \frac{q_{\max} \cdot K_L \cdot C_e}{1 + K_L \cdot C_e} \tag{4}$$

$$q_e = K_f \cdot C_e^{\frac{1}{n}} \tag{5}$$

where c_e (mg/L) is the equilibrium concentration of adsorbate, q_e (mg/g) is the equilibrium amount of adsorbate in the adsorbent, k_L (L/mg) is the Langmuir equilibrium adsorption constant related to the energy of adsorption, q_{max} (mg/g) is the maximum adsorption capacity for mono-layer adsorption, k_F (L/g) is the Freundlich equilibrium constant, and n ($[L/mg]^{1/n}$) is a constant related to the energy of adsorption intensity.

Figure 9A displays the Langmuir and Freundlich isotherm models fit to the experimental phosphate adsorption data for AC@$MgFe_2O_4$-LDO at pH 5. The fitting parameters K_F, $1/n$, q_{max}, K_L, and the associated correlation coefficients of the model fits are presented in Table 2. The Langmuir model fit the experimental data well, with a correlation coefficient of r^2 ~0.99 and a maximum adsorption capacity (q_{max}) of 25.81 mg/g. The current q_{max} value for AC@$MgFe_2O_4$-LDO is comparable to or greater than the maximum adsorption capacities of several metallic ferrite-based adsorbents reported.[2,61,62]

The Langmuir isotherm better fit the monolayer sorption on the finite sites and suggested that the energies of sorption on the surface were uniform and that

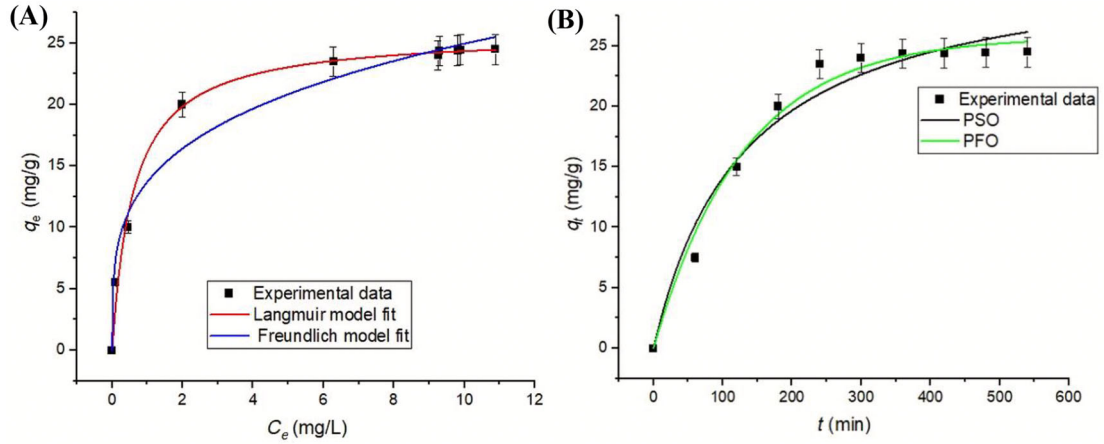

FIGURE 9 (A) The Langmuir and Freundlich isotherm nonlinear curves were fit to the phosphate adsorption experimental data for activated carbon-supported Mg–Fe layered double oxide (AC@$MgFe_2O_4$ LDO) at $T = 30°C$, contact time = 4 h, and adsorbent dose = 4 g/L. (B) The pseudo first order (PFO) and pseudo second order (PSO) kinetic model fits of the phosphate adsorption data at an initial phosphate concentration of 120 mg/L, pH = 5.0, adsorbent dosage = 4.0 g/L, and $T = 30°C$.

TABLE 2 The Langmuir and Freundlich isotherm best fit parameters were used along with the coefficient of determination for phosphate adsorption by the activated carbon-supported Mg–Fe layered double oxide (AC@$MgFe_2O_4$ LDO) composite.

	Langmuir			Freundlich		
Temperature	q_{max} (mg/g)	K_L (Lm/g)	R^2	K_f (L/g)	n	R^2
30°C	25.81	1.66	0.99	27.28	3.85	0.95

no transmigration of sorbate occurred on the surface.[63] Here, the $1/n$ value of 0.259 calculated from the Freundlich model indicates that phosphate adsorption onto the AC@$MgFe_2O_4$-LDH adsorbent was favourable.[63] The steep increase in adsorption capacity observed with the increasing initial phosphate concentration can be attributed to the growing driving force as a result of the higher concentration gradient between the adsorbate on the adsorbent and the adsorbate in the bulk that assists in overcoming mass transfer resistance.[17] The efficiency of the adsorption process in reducing the residual equilibrium phosphate concentration to 0.1 mg/L demonstrates the prominent adsorption performance and phosphate affinity of the adsorbent, demonstrating its robustness in achieving the limit of stringent phosphate effluent concentration recommended by the World Health Organization.[64] The current study revealed high adsorption capacities even at relatively low concentrations, contrary to the findings of several other studies that usually focus on the maximum adsorption capacities observed at relatively high phosphate concentrations, mostly higher than 10 mg/L, which are impractical when dealing with effluent polishing.[56]

The values of the heterogeneity factor ($1/n$) in Table 2 indicate that AC@$MgFe_2O_4$-LDO has a heterogeneous structure. The results show that the value of n is greater than unity, indicating that phosphate is favourably adsorbed by AC@$MgFe_2O_4$-LDO.

3.6 | Adsorption kinetics

A kinetic study is important for determining the adsorbate uptake rate during the adsorption process and for controlling the duration of the entire process.[65] From the experimental data displayed in Figure 9B, it can be observed that there was a steep increase in the adsorption of the phosphate anions during the first 2 h owing to the availability of vacant active sites, which then showed a slightly lower increase in adsorption behaviour until reaching equilibrium after 4 h, after which saturation and equilibrium were reached with no noticeable change in removal percentage. The study of kinetic models is vital because it provides guidance in the design of adsorption systems and provides information about probable adsorption mechanisms involved and adsorption pathways. In light of this, phosphate adsorption kinetics were analyzed using pseudo-first-order and pseudo-second-order models, as presented in Equations (6) and (7), respectively.[65]

TABLE 3 Best-fit kinetic parameters of the pseudo first-order and pseudo second-order kinetic models for phosphate adsorption by activated carbon-supported Mg–Fe layered double oxide (AC@$MgFe_2O_4$ LDO) at $T = 30°C$, pH = 5.0, adsorbent dosage = 4.0 g/L, and adsorption time = 6 h.

	Pseudo first order			Pseudo second order		
Temperature	**q_e (mg/g)**	**K_1 (1/min)**	**R^2**	**q_e (mg/g)**	**K_2 (g/mg min)**	**R^2**
30°C	25.74	0.0077	0.98	32.49	0.00024	0.96

$$q_t = q_e\left(1 - e^{-K_1 t}\right) \tag{6}$$

$$q_t = \frac{q_e^{\,2} K_2\, t}{1 + K_2 q_e t} \tag{7}$$

where q_e (mg/g) and q_t (mg/g) are the amount of adsorbed phosphate at equilibrium and time t, respectively; K_1 (min^{-1}), C_e equilibrium concentration (mg/L^{-1}); and K_2 (g/mg^{-1})$\cdot min^{-1}$ are the rate constants of the pseudo-first-order model and pseudo-second-order model, respectively. The kinetic model best fits the experimental data presented in Figure 9B. The corresponding best-fit kinetic model parameters are provided in Table 3.

Both the PFO and PSO kinetic data models fit the experimental data well, with coefficient of determination values of $r^2 \simeq 0.98$ and $r^2 \simeq 0.975$, respectively, suggesting that the adsorption process is complex.[66] The substantial adsorption of phosphate within the first 2 h could be attributed to the availability of high adsorption sites and electrostatic attraction because of the pH-dependent surface charge and protonation of the adsorbent, which give rise to high affinity for the phosphate anions and reach equilibrium within a few hours.[67] Diffusion processes usually limit the rate of adsorption toward the external adsorbent surface and within porous adsorbent particles.[67] Several studies have shown that porous adsorbents with remarkably high surface areas exhibit low adsorption of anions, even after functionalization with iron oxide nanoparticles, as the majority of the surface area comes from micropores (pore width <2 nm), which may take several days due to a pressure drop. In the present study, 99% phosphate adsorption was achieved in less than 4 h, as the porous structured AC@$MgFe_2O_4$-LDO adsorbent consisted of a network of interconnected macropores and mesopores providing ideal adsorption sites for phosphate anions, as observed from the size distribution analysis in Figure 3B.

3.7 | Intra-particle diffusion model

Understanding the dynamic behaviour of an adsorption system is pivotal for effective design and control of treatment processes. Adsorption is a multistep process, and intraparticle diffusion becomes the rate-determining step when the adsorption process is carried out in a rapidly stirred batch system.[68] The interparticle diffusion model proposed by Morris and Webber[69] is employed to investigate the mechanism of phosphate adsorption and the rate-controlling step of the adsorption process (Equation (8)).[70]

$$q_t = K_{\text{dif}} \times t^{1/2} + C \tag{8}$$

where q_t(mg/g) is the adsorption capacity at time t (min), K_{dif} is the intraparticle diffusion rate constant ($mg/g\ min^{1/2}$), and C (mg/g) is a constant related to the thickness of the boundary layer.

The experimental data for phosphate adsorption onto AC@$MgFe_2O_4$-LDO were fitted to the intraparticle diffusion model, and the parameters K_{dif} and C were determined (Figure 10A). The model fit the experimental data well ($r^2 \simeq 0.89$), and the values of K_{dif} and C were determined to be $0.96\ mg/g \cdot min^{1/2}$ and 5.18 mg/g, respectively. The value of the intercept is indicative of the boundary layer thickness, i.e., with a large intercept, a greater boundary layer effect is observed.[71] In accordance with intraparticle diffusion model theory, if the plot of q_t versus $t^{1/2}$ shows a linear relationship, then intraparticle diffusion is involved in the adsorption process, and it would be the controlling step if the line passes through the origin.[70] As presented in Figure 10B, the linear regression plot of q_t versus $t^{1/2}$ exhibited a linear relationship ($R^2 \simeq 0.99$), indicating that intraparticle diffusion is involved in the adsorption process. However, the plot does not pass through the origin, indicating that the adsorption process is controlled not only by intraparticle diffusion or micropore diffusion but also by boundary layer diffusion or the macropore diffusion effect.[72]

3.8 | Thermodynamics study

The effect of temperature on the adsorption performance was evaluated at various temperatures, as temperature affects the adsorbent's performance by governing its thermodynamic properties. An endothermic process leads

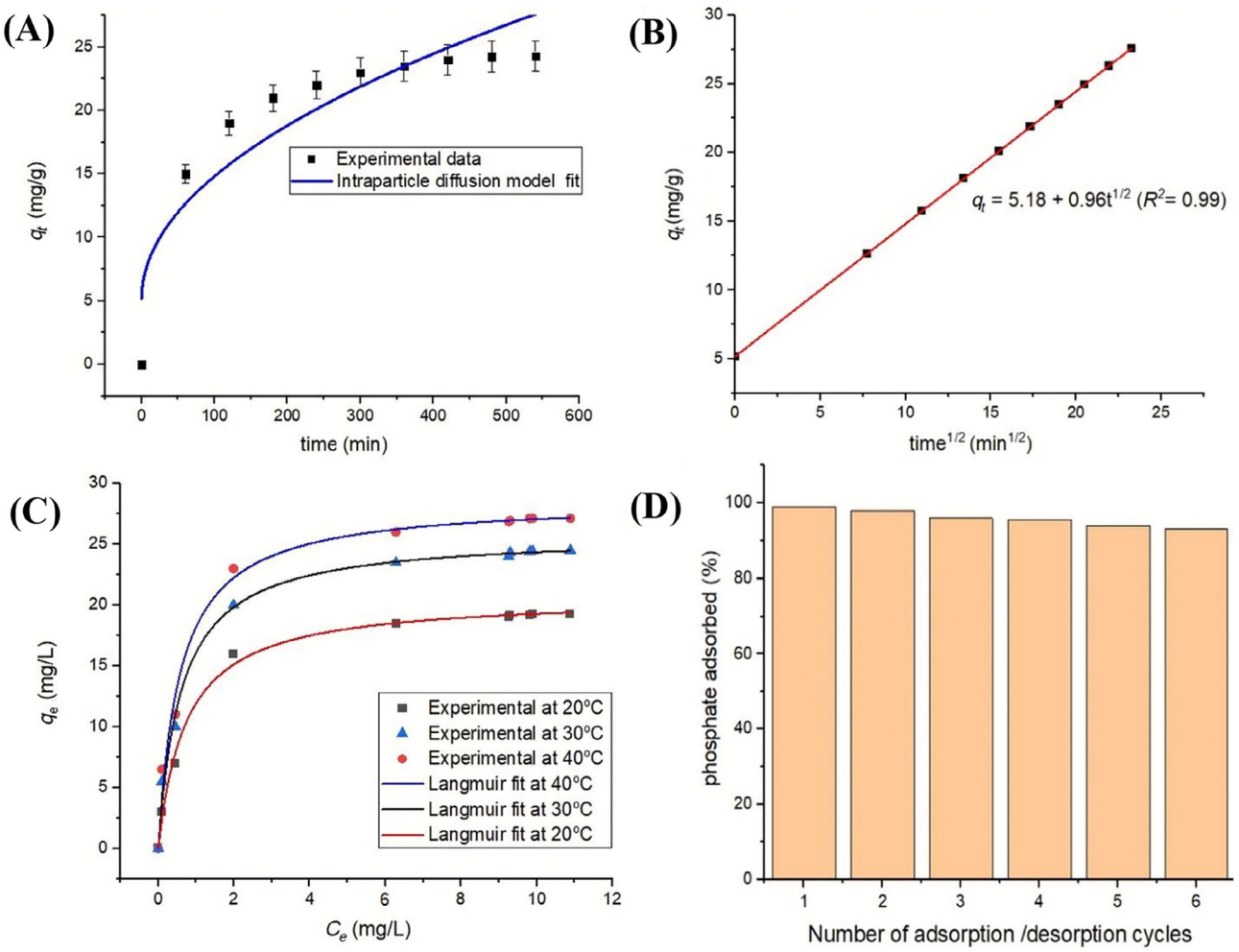

FIGURE 10 (A) Intraparticle diffusion model fit to the experimental data; (B) linear plot of q_t versus $t^{1/2}$. Phosphate adsorption tests carried out with an initial phosphate concentration of 120 mg/L, pH = 5.0, adsorbent dosage = 4.0 g/L, and T = 30°C. (C) Effect of temperature on the phosphate adsorption performance of the activated carbon-supported Mg–Fe layered double oxide (AC@$MgFe_2O_4$ LDO) adsorbent (pH = 5, adsorbent dose = 4 g/L, initial phosphate concentration = 120 mg/L, and T = 20, 30, and 40°C); (D) phosphate desorption and regeneration potentials of the AC@$MgFe_2O_4$-LDO adsorbent observed during cycles of adsorption/desorption at 120 mg/L initial phosphate concentration, pH 5, and an adsorption time of 540 min.

to improved adsorption at higher temperatures, while an exothermic process leads to the opposite results.[56] Phosphate adsorption by the AC@$MgFe_2O_4$-LDO nanocomposites increased with increasing temperature from 20 to 40°C, as shown in Figure 10C.

Table 4 presents the Langmuir model fit parameters and their associated correlation coefficients (r^2) at various temperatures. The study revealed a 37.8% increase in the maximum adsorption capacity (q_{max}) of the adsorbent with increasing solution temperature from 20 to 40°C.

Sorption behaviour can be obtained from thermodynamic parameters such as changes in Gibb's energy change (ΔG^o), changes in enthalpy (ΔH^o), and changes in entropy (ΔS^o) associated with the uptake process. Thermodynamic parameters are important in 'determining the feasibility and spontaneity of an adsorption process. They are also vital in estimating adsorptive mechanisms (i.e., physisorption, ion exchange, or chemisorption)'.[73] Adsorption isotherms obtained at

TABLE 4 Best fit parameters of the Langmuir adsorption isotherm of phosphate by the activated carbon-supported Mg–Fe layered double oxide (AC@$MgFe_2O_4$ LDO) adsorbent at different temperatures.

	Langmuir model fit		
Temperature	**q_{max} (mg/g**	**K_L (L/mg)**	**R^2**
20°C	20.69	1.36	0.99
30°C	25.81	1.66	0.99
40°C	28.42	1.78	0.99

TABLE 5 Thermodynamic parameters for phosphate adsorption by the activated carbon-supported Mg–Fe layered double oxide ($AC@MgFe_2O_4$ LDO) adsorbent.

Temperature (K)	K_c	ΔG^O (kJ mol^{-1})	ΔH^O (kJ mol^{-1})	ΔS^O (kJ mol^{-1} K^{-1})
293.15	7,400,303	−38.6	10.895	0.166
303.15	9,039,618	−40.4		
313.15	9,697,737	−41.9		

different temperatures were used to determine thermodynamic parameters according to Equations (8)–(11).[73]

$$\Delta G^{\circ} = \Delta H^{\circ} - T\Delta S^{\circ} \quad (9)$$

$$\Delta G^{\circ} = -RT \ln K_C \quad (10)$$

The thermodynamic enthalpy change (ΔH) and entropy change (ΔS) parameters were determined using the Van't Hoff equation, as represented by Equation (11):

$$\mathrm{Ln}K_C = \Delta S^{\circ}/R - \Delta H^{\circ}/RT \quad (11)$$

where ΔG° is the Gibbs energy (kJ mol^{-1}), R is the universal gas constant (kJ mol^{-1}/K), T is the temperature (K), ΔH is the enthalpy change, and K_C is the standard equilibrium constant. The values of K_C used in this work were obtained using the Langmuir constant K_L at the specified temperatures. The thermodynamic parameters are strongly dependent on the dimensionless thermodynamic equilibrium constant K_C. This thermodynamic equilibrium constant K_C can be obtained from the constants of various isotherm models, such as the Langmuir and Freundlich models. However, as K_C must be dimensionless, the K_L obtained from the Langmuir isotherm (L/mg) is multiplied by 1000 to convert L/mg into L/g according to the molecular weight of the adsorbate (g/mol) and the unitary standard concentration of the adsorbate (1 mol /L) (making it dimensionless).[74] Thus, the K_C values were obtained from the K_L values, as presented in Table 5. The ΔH° and ΔS° values were determined from the straight-line plot of ln K_C versus $1/T$ and are presented in Table 5.

Phosphate adsorption to the $AC@MgFe_2O_4$-LDO adsorbent increased with increasing temperature from 20 to 40°C (Figure 10C). A positive ΔH° (10.895 kJ mol^{-1}) indicates that the phosphate adsorption process is endothermic, and a negative Gibbs free energy indicates that the process is spontaneous. The positive value of ΔS° (0.166 kJ mol^{-1} K^{-1}) demonstrated the affinity of the sorbent for the sorbate, the increased randomness at the solid–liquid interface, the increased degree of freedom of the sorbate, and the more favourable conditions for the occurrence of the adsorption process.[75] Moreover, the negative values of ΔG° (−38.6 to −41.9 kJ mol^{-1}) suggest that the phosphate ion adsorption process on the $AC@MgFe_2O_4$-LDO adsorbent is spontaneous. Yoon et al.[76] reported similar results for endothermic phosphate adsorption on iron (hydr)oxide adsorbents. In adsorption studies, it is essential to establish adsorption mechanisms (i.e., chemical or physical). A lower enthalpy, which is less than 40 kJ mol^{-1}, indicates physisorption of the adsorbate, which is weakly immobilized on the surface due to van der Waals or dipole interactions, unlike chemical adsorption (or chemisorption), which involves stronger chemical interactions (chemical bonding) involving the transfer of electrons between the adsorbent and adsorbate.[77]

3.9 | Proposed mechanisms of phosphate adsorption

FTIR analysis was carried out before and after the phosphate adsorption process to study the mechanism of phosphate adsorption. As displayed in Figures 2 and S2, the major functional groups observed in the pristine AC were maintained in the $AC@MgFe_2O_4$-LDO nanocomposite. The surface of $AC@MgFe_2O_4$-LDO was observed to have diverse oxygen-containing functional groups, such as carboxylic acid anhydrides, phenols, and ethers (1028 cm^{-1}). As revealed in Figure 2, these peaks are broad and predominant, and it can be inferred that the peaks are actively involved in phosphate adsorption, as they disappear in the adsorbent FTIR spectra after adsorption (Figure 2). The vibrational peaks at ∼890 and 481 cm^{-1} for the hydroxyl groups bound to the metallic surface disappeared after adsorption. On the other hand, the FTIR spectrum of $AC@MgFe_2O_4$-LDO displayed a new peak at 1006 cm^{-1} (Figure S3), which can be ascribed to the bending vibration of the P—O bond,[78,79] confirming that anionic exchange occurred between the hydroxyl groups bound to the $MgFe_2O_4$-LDO and the phosphate anions during the adsorption process. The adsorption mechanism is proposed to be predominantly electrostatic attraction between phosphate ions ($H_2PO_4^-$, HPO_4^{2-}, and PO_4^{3-}) and the protonated surface of the adsorbent at pH values lower than the point of zero charge (pH).[79] The other proposed mechanism involved

in adsorption is ligand exchange between phosphate anions and the hydroxyl ions of AC@$MgFe_2O_4$-LDO.[78] Phosphate binding by AC@$MgFe_2O_4$-LDO through inner-sphere complex formation is also the other probable mechanism of phosphate adsorption.[79]

3.10 | Phosphate recovery and adsorbent regeneration

Phosphate desorption and adsorbent regeneration were efficiently performed by eluting the adsorbent with 1 M NaOH at pH 13. After six cycles of adsorption/desorption, the phosphate adsorption efficiency of the adsorbent decreased by only ~7%, as presented in Figure 10D. The underlying mechanisms that play a major role in phosphate desorption by NaOH are likely ligand exchange and electrostatic repulsion between the phosphate and the adsorbent surface. In the desorption process, the NaOH hydroxyl groups replace the adsorbed phosphate ions at the binding sites.[28] In combination, at a solution pH of 13, the AC@$MgFe_2O_4$-LDO nanocomposite exists in its deprotonated form (as the pH is much higher than the pH_{PZC}); likewise, at a pH of 13, phosphate exists as an anionic phosphate complex ($H_2PO_4^-$, HPO_4^{2-}, PO_4^{3-}), which is favourable for efficient phosphate desorption due to electrostatic repulsion. The successive regeneration and reusability potential of the AC@$MgFe_2O_4$-LDO nanocomposite make this material a promising candidate for the efficient removal of phosphate from aqueous solutions.

Despite the very high surface area and abundance of functional groups on the AC utilized in the present study, its phosphate adsorption potential was insufficient to reach stringent phosphate discharge limits (Figures S1 and S2). The presence of negatively charged functional groups, such as carboxyl and phenolic groups, causes a net negative surface charge, offering only limited capacity to adsorb phosphate oxyanions ($H_2PO_4^-$, HPO_4^{2-}, and PO_4^{3-}). This study demonstrated that surface modification of the predominantly negatively charged surface of AC with layered double hydroxides (LDOs) was highly efficient at removing phosphate. Several studies have reported similar approaches for surface modification of AC with metallic cations or LDHs that have high phosphate affinities and anion binding sites.[14,50,51,79] These results are comparable to previous phosphate adsorption results reported[14,50,51,79]. Wu et al.[50,51] reported that surface modification of biochar with MgO endowed it with high phosphate affinity and was capable of attaining remarkable phosphate adsorption over a broad pH range. Post adsorption morphological characterization carried out after regeneration and calcination displayed porous morphology, displaying the adsorbent's preservation of its original porosity for subsequent adsorption process (Figure S4A,B).

TABLE 6 Comparison of the maximum phosphate adsorption capacity (q_{max}) with that of other adsorbents reported in the literature.

Adsorbent	Adsorption capacity	References
Mg–Fe LDHs-loaded biochar	17.5 mg/g	Bolbol et al.[80]
Zn-Al-layered double hydroxides	17.82–27.10 mg/g	Cheng et al.[81]
Mn/Al double oxygen biochar	28.2 mg/g	Peng et al.[14]
Mg/Ca-modified biochars	129.79 mg /g	Fang et al.[82]
MgO-loaded and sodium alginate-immobilized bentonite beads	70.5 mg/g	Xi et al.[13]
Fe (III)-doped activated carbon	14.12 mg/g	Wang et al.[83]
Phenolic-rich bio-oil and magnetic biochar	64.4 mg/g	Mohamed et al.[11]
Calcined MgMn-LDHs	7.3 mg/g	Chitrakar et al.[84]
$MgFe_2O_4$-biochar-based lanthanum alginate beads	23.76 mg/g	Wang et al.[25] and Wang et al.[24]
Biochar/layered double oxide (LDO)	127.23–132.80 mg/g	Zhang et al.[6]
Zn–Al LDHs and their calcined products (LDOs)	54.1–232 mg/g	Zhou et al.[12]
Zn-Al LDH	2.6–2.72 mmol/g	Iftekhar et al.[19]
Biochar/MgAl-LDH	410 mg/g	Zhang et al.[21]
Fe_3O_4@SiO_2 core/shell functionalized with hydrous lanthanum oxide	27.8 mg/g	Lai et al.[61]
Lanthanum-doped biochar (La/Fe_3O_4-BC) Cerium-doped biochar (Ce/Fe_3O_4-BC)	20.5 mg/g 12.5 mg/g	Wang et al.[62] Wang et al.[62]
Activated carbon supported/$MgFe_2O_4$	25.81 mg/g	Current study

Despite the persistent advancement and exploration of efficient adsorbents for the complete mitigation of phosphate and avoidance of eutrophication, the development of a robust phosphate adsorbent with high adsorption potential and strong selectivity, abundant binding sites, high phosphate affinity, and the ability to meet the stringent permissible discharge limits of the EU is currently challenging. The novelty of the current work lies in the robustness of the adsorbent to achieve nearly complete phosphate adsorption over a broad pH range (4–9), its high regeneration potential, and its strong selectivity for phosphate despite the slight competition of highly negatively charged sulphate ions, demonstrating its potential viability for scalability and practical application in real-world complex aqueous matrices. The decrease in the residual equilibrium phosphate concentration to as low as 0.1 mg/L revealed the efficient adsorption potential and phosphate affinity of the adsorbent, demonstrating its potential to meet the stringent phosphate effluent concentration limit of the World Health Organization.[64] The current study displayed high adsorption capacity even at lower concentrations, contrary to the reports of several studies usually focusing on the maximum adsorption capacities observed at higher phosphate concentrations, mostly concentrations higher than 10 mg/L, which are unrealistic when dealing with effluent polishing.[56] The efficient adsorption potential can be ascribed to the high surface area, mesoporous structure, and high point of zero charge that contributed to the efficient abatement of phosphate-contaminated aqueous solution. The prominent phosphate adsorption performance of the adsorbent can be attributed to the synergistic merits of the abundant functional groups and mesoporous structure of the AC matrix coupled with a high point of zero charge (pHpzc) owing to the positive charge of the LDH (pH = 9.8) and the high positive charge of the LDH. The current AC@Mg-Fe_2O_4-LDO adsorbent is comparable to several LDH-based phosphate adsorbents reported in the literature, as presented in Table 6. The efficient phosphate adsorption potential of the adsorbent over a broad pH range demonstrated the scalability and real-world application potential of the novel adsorbent for large-scale utilization of phosphate abatement from contaminated aqueous media.

4 | CONCLUSIONS

In the present study, a novel AC-supported ($MgFe_2O_4$-LDO (AC@) $MgFe_2O_4$-LDO) was synthesized with the remarkable potential for anionic phosphate adsorption from contaminated water over a wide pH range. The porous AC@$MgFe_2O_4$-LDO, which has a mesoporous structure and uniform size distribution, demonstrated an appropriate adsorbent dose and temperature-dependent removal of phosphate ions over a wide pH range (4–9) with high buffering capacity. The adsorbent achieved up to 99% removal of phosphate at a 4 g/L dose within 4 h of adsorption, and the phosphate adsorption capacity increased by 33% with increasing adsorption temperature from 20 to 40°C. The adsorption isotherm followed the Langmuir model with a maximum adsorption capacity of 25.81 mg/g. The kinetic data were best fitted with both first-order pseudo kinetic and second-order pseudo-kinetic models demonstrating complex adsorption processes involving both physisorption of the adsorbate, which was weakly immobilized on the surface due to van der Waals or dipole interactions, and chemisorption of the adsorbate. A thermodynamic study revealed that the phosphate adsorption process is endothermic, spontaneous, and favourable. The novelty of the current work lies in the robustness of the adsorbent to achieve nearly complete phosphate adsorption over a broad pH range (4–9), its high regeneration potential, and its strong selectivity for phosphate despite the slight competition of highly negatively charged sulphate ions, demonstrating its potential viability for scalability and practical application in real-world complex aqueous matrices. The results of this study demonstrated that the high surface area, well-developed porosity, high anion exchange, and pH buffering capacities of AC@$MgFe_2O_4$-LDO might be useful for phosphate adsorption and recovery from contaminated water bodies.

AUTHOR CONTRIBUTIONS

Fisseha A. Bezza: Conceptualization; methodology; investigation; formal analysis; writing – review and editing; writing – original draft; data curation. **Hendrik G. Brink:** Writing – review and editing; formal analysis; funding acquisition. **Evans M. N. Chirwa:** Funding acquisition; validation; project administration; writing – review and editing.

ACKNOWLEDGEMENTS

This work was supported by the Water Research Commission (WRC) research fund and the National Research Foundation (NRF) of South Africa through the Incentive Funding for Rated Researchers Grant No. IFR200206501999, awarded to Prof. Evans M. N. Chirwa of the University of Pretoria. The work further received support from the Austrian Federal Ministry of Education, Science and Research (BMBWF) through Austria's Agency for Education and Internationalization (OeAD) (Grant Numbers: Africa UNINET P058 and APPEAR Project 341).

CONFLICT OF INTEREST STATEMENT

The authors declare no competing interest of any form.

DATA AVAILABILITY STATEMENT

All data generated or analyzed during this study are included in this published article and its supplementary information files.

ORCID

Fisseha A. Bezza https://orcid.org/0000-0003-4649-3165

REFERENCES

[1] H. A. Loomer, S. E. Cooke, *Water Quality in the Grand River Watershed: Current Conditions and Trends (2003–2008)*, Grand River Conservation Authority, Cambridge, ON **2015**.
[2] W. Gu, X. Li, M. Xing, W. Fang, D. Wu, *Sci. Total Environ.* **2018**, *619*, 42.
[3] H. Huang, J. Liu, L. Ding, *J. Cleaner Prod.* **2015**, *102*, 437.
[4] M. Li, J. Liu, Q. Zhou, M. Gifford, P. Westerhoff, *J. Cleaner Prod.* **2019**, *217*, 127.
[5] M. Hasan, M. Khalekuzzaman, N. Hossain, M. Alamgir, *J. Cleaner Prod.* **2021**, *292*, 126042.
[6] Z. Zhang, L. Yan, H. Yu, T. Yan, X. Li, *Bioresour. Technol.* **2019**, *284*, 65.
[7] J. U. Kaljunen, R. A. Al-Juboori, A. Mikola, I. Righetto, I. Konola, *J. Cleaner Prod.* **2021**, *281*, 125288.
[8] R. Bashar, K. Gungor, K. G. Karthikeyan, P. Barak, *Chemosphere* **2018**, *197*, 280.
[9] Y. Peng, Y. Sun, R. Sun, Y. Zhou, D. C. Tsang, Q. Chen, *J. Cleaner Prod.* **2019**, *237*, 117770.
[10] Z. Wang, D. Shen, F. Shen, T. Li, *Chemosphere* **2016**, *150*, 1.
[11] B. A. Mohamed, Z. Liu, X. Bi, L. Y. Li, *J. Cleaner Prod.* **2022**, *333*, 130090.
[12] J. Zhou, S. Yang, J. Yu, Z. Shu, *J. Hazard. Mater.* **2011**, *192*, 1114.
[13] H. Xi, H. Jiang, D. Zhao, A. H. Zhang, B. Fan, Y. Yang, J. Zhang, *J. Cleaner Prod.* **2021**, *313*, 127773.
[14] G. Peng, S. Jiang, Y. Wang, Q. Zhang, Y. Cao, Y. Sun, W. Zhang, L. Wang, *J. Cleaner Prod.* **2020**, *251*, 119725.
[15] K. Rybka, J. Matusik, M. Marzec, *J. Cleaner Prod.* **2022**, *332*, 130084.
[16] Y. Peng, Y. Sun, A. Hanif, J. Shang, Z. Shen, D. Hou, Y. Zhou, Q. Chen, Y. S. Ok, D. C. Tsang, *J. Cleaner Prod.* **2021**, *289*, 125142.
[17] K. W. Jung, S. Y. Lee, J. W. Choi, M. J. Hwang, W. G. Shim, *Chem. Eng. J.* **2021**, *420*, 129775.
[18] D. Kang, X. Yu, S. Tong, M. Ge, J. Zuo, C. Cao, W. Song, *Chem. Eng. J.* **2013**, *228*, 731.
[19] S. Iftekhar, M. E. Küçük, V. Srivastava, E. Repo, M. Sillanpää, *Chemosphere* **2018**, *209*, 470.
[20] L. Xue, B. Gao, Y. Wan, J. Fang, S. Wang, Y. Li, R. Muñoz-Carpena, L. Yang, *J. Taiwan Inst. Chem. Eng.* **2016**, *63*, 312.
[21] M. Zhang, B. Gao, Y. Yao, M. Inyang, *Chemosphere* **2013**, *92*, 1042.
[22] B. A. Jiménez-López, R. Leyva-Ramos, J. J. Salazar-Rábago, A. Jacobo-Azuara, A. Aragón-Piña, *Environ. Nanotechnol., Monit. Manage.* **2021**, *16*, 100580.
[23] Y. Zhang, D. Lv, J. Chen, Z. Liu, C. Duan, X. Chen, W. Yuan, H. Xi, Q. Xia, *New J. Chem.* **2021**, *45*, 8045.
[24] L. Wang, J. Wang, W. Yan, C. He, Y. Shi, *Chem. Eng. J.* **2020**, *387*, 123305.
[25] Z. Wang, S. Bakshi, C. Li, S. J. Parikh, H. S. Hsieh, J. J. Pignatello, *J. Colloid Interface Sci.* **2020**, *579*, 258.
[26] S. Bakshi, D. A. Laird, R. G. Smith, R. C. Brown, *ACS Sustainable Chem. Eng.* **2021**, *9*(2), 658.
[27] M. Park, S. Wu, I. J. Lopez, J. Y. Chang, T. Karanfil, S. A. Snyder, *Water Res.* **2020**, *170*, 115364.
[28] A. Zach-Maor, R. Semiat, H. Shemer, *J. Colloid Interface Sci.* **2011**, *363*, 608.
[29] Y. Yang, X. Tan, E. Almatrafi, S. Ye, B. Song, Q. Chen, H. Yang, Q. Fu, Y. Deng, Z. Zeng, G. Zeng, *Sci. Total Environ.* **2022**, *844*, 156835.
[30] H. Shao, J. Wu, S. Wang, J. Duan, Y. Zhang, J. Peng, T. Lin, *Ceram. Int.* **2022**, *48*, 7183.
[31] T. T. Win, S. Khan, B. Bo, S. Zada, P. Fu, *Sci. Rep.* **2021**, *11*, 21996.
[32] Z. Chai, Q. Tian, J. Ye, S. Zhang, G. Wang, Y. Qi, Y. Che, G. Ning, *J. Mater. Sci.* **2020**, *55*, 4408.
[33] F. Millange, R. I. Walton, D. O'Hare, *J. Mater. Chem.* **2000**, *10*, 1713.
[34] S. B. Lee, E. H. Ko, J. Y. Park, J. M. Oh, *Nanomaterials* **2021**, *11*, 1153.
[35] B. K. Labde, M. C. Sable, N. R. Shamkuwar, *Mater. Lett.* **2003**, *57*, 1651.
[36] M. Kazayawoko, J. J. Balatinecz, R. T. Woodhams, *J. Appl. Polym. Sci.* **1997**, *66*, 1163.
[37] S. Parlayici, V. Eskizeybek, A. Avcı, E. Pehlivan, *J. Nanostruct. Chem.* **2015**, *5*, 255.
[38] S. M. Yakout, G. S. El-Deen, *Arabian J. Chem.* **2016**, *9*, S1155.
[39] O. Levy-Ontman, O. Paz-Tal, Y. Alfi, A. Wolfson, *RSC Adv.* **2023**, *13*, 35831.
[40] A. M. Abdelghany, M. S. Meikhail, A. H. Oraby, M. A. Aboelwafa, *Polym. Bull.* **2023**, *80*, 13279.
[41] O. Togibasa, Y. O. Ansanay, K. Dahlan, M. Erari, *Journal of Physics: Theories and Applications* **2021**, *5*, 1.
[42] W. Maulina, R. Kusumaningtyas, Z. Rachmawati, A. Arkundato, L. Rohman, E. Purwandari, *IOP Conference Series: Earth and Environmental Science* **2019**, *239*, 012035.
[43] R. Elangovan, V. Vijayan, S. Bakthavatsalam, K. Ramkumar, T. Sathish, K. Sudhakar, *J. Cluster Sci.* **2023**, *34*, 991.
[44] Y. Li, Z. Yang, Y. Wang, Z. Bai, T. Zheng, X. Dai, S. Liu, D. Gui, W. Liu, M. Chen, L. Chen, *Nat. Commun.* **2017**, *8*, 1.
[45] S. Fu, Q. Fang, A. Li, Z. Li, J. Han, X. Dang, W. Han, *Energy Sci. Eng.* **2021**, *9*, 80.
[46] L. Fan, B. Zhou, S. Zhang, S. Hu, X. Mi, R. Sun, Y. Wu, *Bull. Environ. Contam. Toxicol.* **2021**, *106*, 134.
[47] S. Mor, K. Chhoden, K. Ravindra, *J. Cleaner Prod.* **2016**, *129*, 673.
[48] R. Liu, Z. Yang, G. Wang, J. Xian, T. Li, Y. Pu, Y. Jia, W. Zhou, Z. Cheng, S. Zhang, G. Xiang, *J. Cleaner Prod.* **2021**, *313*, 127945.
[49] Z. Yan, B. Zhu, J. Yu, Z. Xu, *RSC Adv.* **2016**, *6*, 50128.
[50] H. Wu, H. Zhang, W. Zhang, X. Yang, H. Zhou, Z. Pan, D. Wang, *Chemosphere* **2019**, *219*, 66.
[51] L. Wu, C. Wei, S. Zhang, Y. Wang, Y. Kuzyakov, X. Ding, *J. Cleaner Prod.* **2019**, *235*, 901.
[52] G. Y. A. El-Reesh, A. A. Farghali, M. Taha, R. K. Mahmoud, *Sci. Rep.* **2020**, *10*, 1.
[53] B. Gao, P. Li, R. Yang, A. Li, H. Yang, *Sci. Rep.* **2019**, *9*, 1.
[54] P. Huang, Z. Liang, Z. Zhao, F. Cui, *J. Cleaner Prod.* **2021**, *301*, 126976.

[55] E. N. El Qada, S. J. Allen, G. M. Walker, *Chem. Eng. J.* **2006**, *124*, 103.
[56] P. S. Kumar, L. Korving, M. C. van Loosdrecht, G. J. Witkamp, *Water Res: X* **2019**, *4*, 100029.
[57] X. Yang, Y. Wan, Y. Zheng, F. He, Z. Yu, J. Huang, H. Wang, Y. S. Ok, Y. Jiang, B. Gao, *Chem. Eng. J.* **2019**, *366*, 608.
[58] R. Liu, L. Chi, X. Wang, Y. Sui, Y. Wang, H. Arandiyan, *J. Environ. Chem. Eng.* **2018**, *6*, 5269.
[59] G. Li, S. Gao, G. Zhang, X. Zhang, *Chem. Eng. J.* **2014**, *235*, 124.
[60] R. I. Yousef, B. El-Eswed, H. Ala'a, *Chem. Eng. J.* **2011**, *171*, 1143.
[61] L. Lai, Q. Xie, L. Chi, W. Gu, D. Wu, *J. Colloid Interface Sci.* **2016**, *465*, 76.
[62] L. Wang, J. Wang, C. He, W. Lyu, W. Zhang, W. Yan, L. Yang, *Colloids Surf., A* **2019**, *561*, 236.
[63] Q. Y. Yue, W. Y. Wang, B. Y. Gao, X. Xu, J. Zhang, Q. Li, *Water Environ. Res.* **2010**, *82*, 374.
[64] H. N. Tran, S. J. You, A. Hosseini-Bandegharaei, H. P. Chao, *Water Res.* **2017**, *120*, 88.
[65] H. S. Karapınar, *Environ. Technol.* **2021**, *43*, 1.
[66] T. Li, Z. Tong, Q. Zheng, H. Bao, A. Partow, S. Meng, L. Li, Y. C. Li, *ACS Sustainable Chem. Eng.* **2021**, *9*, 10468.
[67] J. Ifthikar, J. Wang, Q. Wang, T. Wang, H. Wang, A. Khan, A. Jawad, T. Sun, X. Jiao, Z. Chen, *Bioresour. Technol.* **2017**, *238*, 399.
[68] M. N. Ismael, A. El Nemr, E. S. H. El Ashry, H. Abdel Hamid, *Environ. Processes* **2020**, *7*, 911.
[69] J. C. Morris, W. J. Webber Jr., in *Advances in Water Pollution Research*, Pergamon, Oxford **1964**, pp. 231–266.
[70] B. Wang, X. Hu, D. Zhou, H. Zhang, R. Chen, W. Guo, H. Wang, W. Zhang, Z. Hong, W. Lyu, *J. Cleaner Prod.* **2021**, *298*, 126878.
[71] N. Kannan, M. M. Sundaram, *Dyes Pigm.* **2001**, *51*, 25.
[72] M. Pan, X. Lin, J. Xie, X. Huang, *RSC Adv.* **2017**, *7*, 4492.
[73] D. Pang, P. Wang, H. Fu, C. Zhao, C. C. Wang, *Appl. Sci.* **2020**, *2*, 1.
[74] X. Zhou, X. I. N. Zhou, *Chem. Eng. Commun.* **2014**, *201*, 1459.
[75] P. Saha, S. Chowdhury, *Thermodynamics* **2011**, *16*, 349.
[76] S. Y. Yoon, C. G. Lee, J. A. Park, J. H. Kim, S. B. Kim, S. H. Lee, J. W. Choi, *Chem. Eng. J.* **2014**, *236*, 341.
[77] L. A. Rodrigues, L. J. Maschio, R. E. da Silva, M. L. C. P. da Silva, *J. Hazard. Mater.* **2010**, *173*, 630.
[78] M. He, P. Zhang, X. Zhang, F. Li, S. Huo, D. Fang, B. Liang, K. Li, *J. Cleaner Prod.* **2022**, *361*, 132262.
[79] Z. H. Xie, H. Y. Zhou, C. S. He, Z. C. Pan, G. Yao, B. Lai, *Chem. Eng. J.* **2021**, *414*, 128713.
[80] H. Bolbol, M. Fekri, M. Hejazi-Mehrizi, *Arabian J. Geosci.* **2019**, *12*, 1.
[81] X. Cheng, Y. E. Jiexu, S. Dezhi, C. H. E. N. Aiyan, *Chin. J. Chem. Eng.* **2011**, *19*, 391.
[82] L. Fang, J. S. Li, S. Donatello, C. R. Cheeseman, C. S. Poon, D. C. Tsang, *J. Cleaner Prod.* **2020**, *244*, 118853.
[83] Z. Wang, E. Nie, J. Li, M. Yang, Y. Zhao, X. Luo, Z. Zheng, *Environ. Sci. Pollut. Res.* **2012**, *19*, 2908.
[84] R. Chitrakar, S. Tezuka, A. Sonoda, K. Sakane, K. Ooi, T. Hirotsu, *J. Colloid Interface Sci.* **2005**, *290*, 45.

SUPPORTING INFORMATION

Additional supporting information can be found online in the Supporting Information section at the end of this article.

How to cite this article: F. A. Bezza, H. G. Brink, E. M. N. Chirwa, *Can. J. Chem. Eng.* **2024**, 1. https://doi.org/10.1002/cjce.25440